Measurement of the x-ray mass attenuation coefficient and determination of the imaginary component of the atomic form factor of tin over the energy range of 29–60 keV

Martin D. de Jonge

X-Ray Operations and Research, Argonne National Laboratory, 9700 South Cass Avenue, Argonne, Illinois 60439, USA

Chanh Q. Tran, Christopher T. Chantler, Zwi Barnea, and Bipin B. Dhal

School of Physics, University of Melbourne, Victoria 3010, Australia

David Paterson

Australian Synchrotron Project, Major Projects Victoria, 800 Blackburn Road, Clayton, Victoria 3168, Australia

Elliot P. Kanter, Stephen H. Southworth, and Linda Young

Chemistry Division, Argonne National Laboratory, 9700 South Cass Avenue, Argonne, Illinois 60439, USA

Mark A. Beno, Jennifer A. Linton, and Guy Jennings

BESSRC-CAT, Argonne National Laboratory, 9700 South Cass Avenue, Argonne, Illinois 60439, USA

We use the x-ray extended-range technique (XERT) [C. T. Chantler *et al.*, Phys. Rev. A **64**, 062506 (2001)] to measure the mass attenuation coefficients of tin in the x-ray energy range of 29–60 keV to 0.04–3 % accuracy, and typically in the range 0.1–0.2 %. Measurements made over an extended range of the measurement parameter space are critically examined to identify, quantify, and correct a number of potential experimental systematic errors. These results represent the most extensive experimental data set for tin and include absolute mass attenuation coefficients in the regions of x-ray absorption fine structure, extended x-ray absorption fine structure, and x-ray absorption near-edge structure. The imaginary component of the atomic form factor f_2 is derived from the photoelectric absorption after subtracting calculated Rayleigh and Compton scattering cross sections from the total attenuation. Comparison of the result with tabulations of calculated photoelectric absorption coefficients indicates that differences of 1–2 % persist between calculated and observed values.

PACS number(s): 32.80.Cy, 61.10.Ht, 32.80.Fb, 78.20.Ci

I. INTRODUCTION

X-ray mass attenuation coefficients are computed from atomic theory, quantum mechanics, and solid-state physics using self-consistent electronic wave functions in order to describe the scattering and absorption of x rays. Major differences in available calculations result from the different theoretical frameworks employed to compute these wave functions, which treat exchange, correlation, and overlap effects differently. Further differences stem from the diverse approximate methods used to describe these multielectronic wave functions.

The attenuation of x rays by materials provides a rich diagnostic tool for testing our understanding of the fundamental properties of matter in the atomic, molecular, or solid state. Relative and absolute measurements of the mass attenuation coefficient test theoretical predictions of photoelectric absorption and form factors [1,2], investigate the dynamics of atomic processes, including shake-up, shake-off, and Auger transitions [3–6], and provide information on the density of electronic states [7], molecular bonding, and other solid-state properties [8]. A full understanding of the interactions between x rays and matter requires accurate measurements so that each contributing process may be compared with theoretical models. Relative attenuation measurements provide crucial information whereas absolute attenuation measurements provide additional demanding tests of theory and computation. For example, finite-difference calculations [9] have recently had significant success in predicting extended x-ray absorption fine structure (EXAFS) on a relative scale [10,11], but are currently in relatively poor agreement with the results of absolute measurements [12]. In turn, recent analyses of highly accurate data are beginning to make inroads into solid-state physics modeling and assumptions [13].

We present in Fig. 1 a comparison between the results of two commonly used tabulations of mass attenuation coefficientsfor tin, FFAST [14–16], and XCOM [17,18]. These results have been derived directly from form-factor calculations including estimates of small Rayleigh and Compton scattering contributions. The ordinate of this plot is the percentage difference from the FFAST tabulation [14–16]. This figure shows modest differences between the two tabulations. Although much smaller, the pattern of the differences is similar in form to the case of molybdenum [20], indicating that a common theoretical limitation may be responsible. The only other element exhibiting a similar above-edge discrepancy in the 10–50 keV energy range is tin [19], and so this element presents a good opportunity to support the observation of the molybdenum measurement and therefore to isolate the cause of the difference.

These models and their implementations can in principle be tested by comparing tabulated and measured values. Fig.
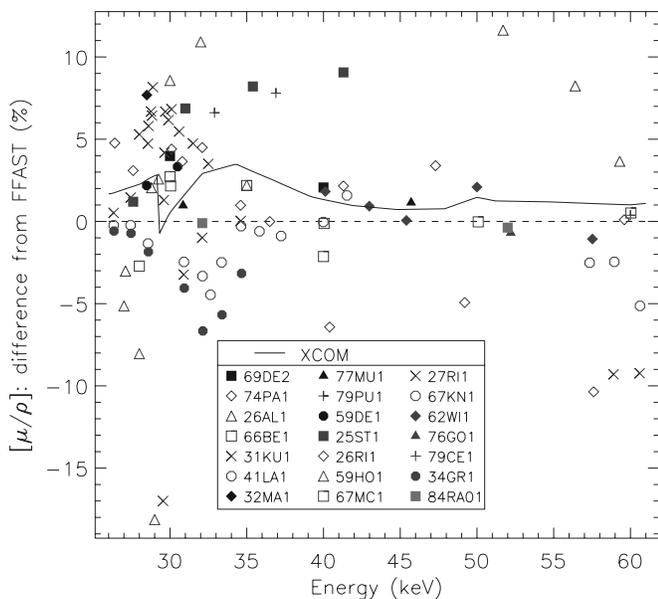
FIG. 1. Discrepancies between theoretical predictions and experimental measurements of the mass attenuation coefficientof tin presented as a percentage difference from the FFAST tabulation [14–16]. The XCOM tabulation is from [17,18]. The various previously measured values have been sourced from the compilation of Hubbell *et al.* [21,22] whose symbols we retain. Mean attenuation coefficients obtained in the same experiment are marked by the same symbol. The 10–20 % variation between the measured values whose typical claimed uncertainties are around 2% indicates the presence of unquantified errors affecting these measurements.

1 includes the results of a number of measurements of the mass attenuation coefficient of metallic tin [21,22]. We see immediately that the large scatter of the measurements does not make it possible to compare them with either tabulation. These reported measurements typically claim accuracies of 0.5–2 %, which should be sufficient to decide between the theoretical computations. However, despite these claimed accuracies, the different sets of measurements disagree with one another by up to 20%. In order to discriminate between the different tabulated values, measurements are required to be accurate and precise to better than about 1% in the region of the absorption edge and to better than 0.2% at energies above about 40 keV.

The discrepancies between the theories, between different experiments, and between theory and experiment have prompted the International Union of Crystallography, representing one of the world's largest group of users of form-factor data, to undertake a systematic investigation of form-factor-based calculations of mass attenuation coefficients and their measurement [23,24]. The principal conclusion of their survey of measurement techniques was that a variety of poorly understood and unquantified sources of systematic error may be adversely affecting the measurements.

The x-ray extended-range technique (XERT) [1,2,25] employs measurements made over an extended range of the measurement parameter space to probe systematic errors affecting the measurements. The specific extended ranges of the measurement parameter space investigated included the attenuation $\left[\frac{\mu}{\rho}\right][\rho t]$ of the absorbers, the x-ray energy, the

angular acceptance of the detectors, the angle of the absorbing sample relative to the incident x-ray beam, and the variations in the integrated column density of the absorbing foil. These parameter-space explorations sought the optimal measurement configuration but were deliberately extended outside the optimal regimes to determine the effect of systematic errors on the measurement.

Earlier studies have focused on low energies and low atomic numbers. The experimental techniques have required significant development for application to higher energies and to higher atomic number for tin, and we report the key aspects of this.

We have investigated silicon at low and intermediate energies in the past [2(b)]. Interestingly, the study of the higher energies for silicon has been quite anomalous [2(c)] and we are also interested to investigate whether tin shows the same qualitative anomaly at high energies or whether this might possibly relate to low atomic number materials or the nature of the band structure, for example.

Of course, as just stated, tin has 15% discrepancies and scatter among the experimental literature. By addressing appropriate experimental techniques for this element and energy range we may therefore address key and possible general experimental issues for the field.

In this article we report measurements of the mass attenuation coefficients of tin. The results of an extensive investigation of systematic errors affecting the measurement are presented. The mass attenuation coefficients are determined to accuracies of between 0.04% and 1% in the neighborhood of the K-absorption edge at about 29.2 keV, rising smoothly to about 1% at 60 keV. The precision (self-consistency) of the measurements is 0.04–3 % at 294 energies between 29 keV and 60 keV.

This article is divided into eight sections. In Sec. II we describe the attenuating samples and the experimental setup. Sec. III describes the detailed interpretation of the measurements leading to the determined mass attenuation coefficients. In Sec. IV we report the method by which we determine the energy of the attenuated x rays. Section V describes the treatment of six measurements made using x rays whose energy was equal to $\frac{3}{4}$ of the desired value. These accidental measurements provide a fortuitous "blind" test of the accuracy of the measurement. We provide a tabulation of the results in Sec. VI, and quantify contributions to the accuracy and the precision of the results. In Sec. VII we compare our results with a variety of calculated photoelectric absorption coefficients and find that the currently available tabulations differ significantly from our measured values. Section VIII is a summary of our conclusions.

II. EXPERIMENTAL SETUP

A. Samples

The tin foil samples were of various thicknesses between 25 μm and 500 μm and were all approximately 25 mm × 25 mm in area as supplied by ESPI [26]. The quoted purity of all foils was better than 99.99%. A typical assay provided by the manufacturer listed the impurities as sodium (5 ppm), aluminium (10 ppm), sulphur (30 ppm), chromium (4 ppm),

iron (7 ppm), lead (5 ppm), calcium (30 ppm), and potassium (6 ppm). To these we have added heavy-metal impurities quoted for 99.999%-purity tin foils, being silver (0.1 ppm), bismuth (0.1 ppm), copper (0.2 ppm), indium (2 ppm), magnesium (0.5 ppm), and antimony (2 ppm) [27]. At certain energies these heavy-metal impurities can have a greater impact on the mass attenuation coefficient than the more copious lighter elements. The total effect of the impurities on the measured mass attenuation coefficient was estimated by use of the tabulated values of their mass attenuation and found to be less than 0.003% for all x-ray energies measured in this experiment.

Each foil was weighed to determine its mass m using a microgram-accuracy Mettler microbalance which was buoyancy compensated for a mass of density $\rho = 8.4$ g/cm^3. The residual effect of the buoyancy of the tin samples (nominal density $\rho = 7.3$ g/cm^3) is to alter the apparent mass by around 0.0012%, and this effect was not corrected as it is well below the measurement uncertainty. Each foil had its projected facial area A measured with a Mitutogo PJ300 traveling-stage shadow-projection optical comparator. The mass and area of each foil was used to determine its average integrated column density $\overline{[\rho t]} = \frac{m}{A}$.

B. Experimental components

The x-ray beam was produced by a bending magnet device at the 12-BM XOR beamline [28] of the Advanced Photon Source facility at the Argonne National Laboratory. The photon flux decreases rapidly with increasing photon energy above the synchrotron characteristic energy of about 19 keV. We expect a factor of 4 reduction in the x-ray flux and a factor of 10 reduction in the detector efficiencies upon increasing the energy from 29 keV to 60 keV.

To monochromatize the x-ray beam energy in the range from 29 keV to 60 keV, we first reflected the x-ray beam from a pair of silicon crystals located in the first optical enclosure of the 12-BM facility. The {4,4,4} planes of these crystals were oriented to select the desired photon energy. However, this orientation also permits the diffraction of a harmonic series of energies, passing allowed multiples of the first-order energy. The $(4n-2)$ multiples of the first-order energy are not reflected as they are forbidden for this crystal.

Further monochromation was effected by a second double reflection of the x-ray beam from the {3,3,3} planes of a channel-cut silicon crystal located in the experimental hutch, 10–20 m downstream of the first optical enclosure. The use of reflection orders with no common factors ensures the rejection of all higher-order energy harmonics up to the $4 \times 3 = 12$th-order multiple of the first-order energy. The lowest unwanted energy component passed by this combination of crystals is the third-order multiple of the desired beam energy. Due to the rapid decrease of the detector efficiencies and the bending magnet intensity with increasing energy the effective intensity of this high-energy component is extremely low.

Figure 2 presents a schematic of the experimental setup. After monochromation, the x rays passed through a pair of orthogonal adjustable slits which defined the beam cross sec-
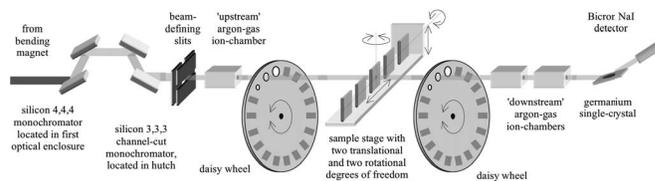

FIG. 2. Schematic of the experimental layout.

tion of approximately 4 mm in the horizontal direction by 1 mm in the vertical direction. These beam dimensions were chosen to optimize the intensity of the x-ray beam used for the measurement. The available x-ray intensity was significantly lower than that reported in another paper [20] because this experiment used a bending-magnet source with a four-reflection monochromating system. Details relating to the sample stage and the measurement sequence and processing are otherwise similar to those described in [20].

The x-ray beam intensities were measured using matched, 260-mm-long argon-gas ion chambers. Argon gas was serially flowed through the detectors at a rate of around 1 l/min. The x-ray energy range covered by this investigation, from 29 keV to 60 keV, includes the K-shell absorption edge of tin at around 29.2 keV. The energy spacing of the measurements was varied in accordance with the structure in the mass attenuation coefficient of tin: it was kept down to 1 eV within 100 eV of the absorption edge, and was increased to 500 eV at energies far from the absorption edge. The sample thicknesses were chosen such that at each energy they typically spanned a range of attenuation $(0.1-0.9) \lesssim \left[\frac{\mu}{\rho}\right][\rho t] \lesssim (2-7.5)$ (see Fig. 3).

Daisy wheels [29] were located between the sample stage and the ion chambers. These had on their perimeters two apertures subtending solid angles of 103 μsr and 464 μsr at the sample, which restricted the flux of scattered or fluorescing photons entering either ion chamber from the sample. In
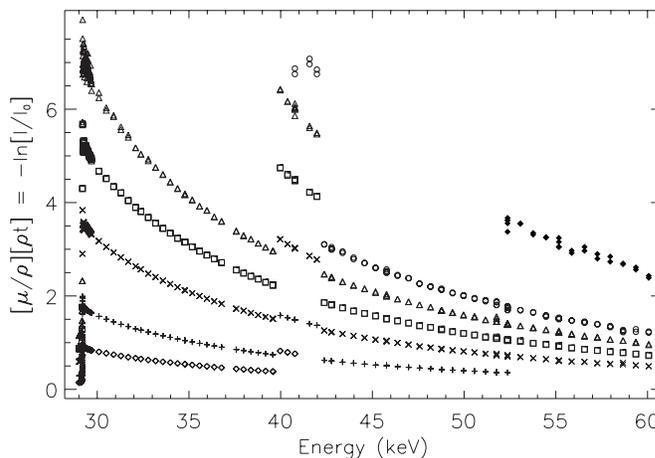

FIG. 3. Measured attenuations $-\ln\left(\frac{I_t}{I_b}\right) = \left[\frac{\mu}{\rho}\right][\rho t]$. The markers represent results obtained using foils of the following nominal thicknesses: $\diamond$, 25 μm; $+$, 50 μm; $\times$, 100 μm; $\square$, 150 μm; $\triangle$, 200 μm; $\bigcirc$, 250 μm; $\blacklozenge$, 500 μm. A subset of the foils was measured at each energy. The absorbers span a wide range of attenuations at each measured energy, allowing attenuation-dependent systematic errors to be detected.
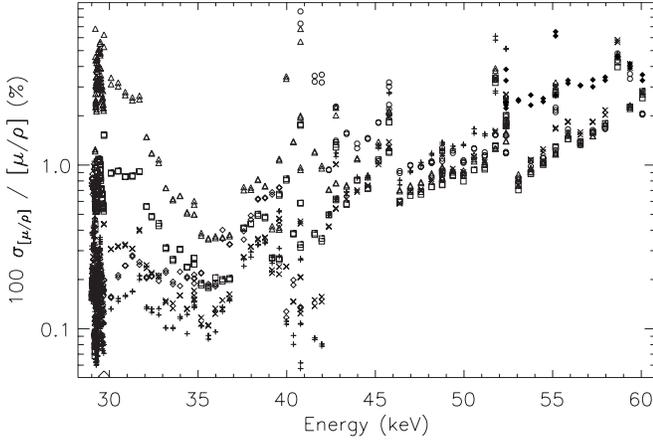
FIG. 4. Precision of the attenuation measurements as dominated by counting statistics recorded by the first downstream ion chamber. The uncertainty of $\left[\frac{\mu}{\rho}\right]$ for the optimum foil thickness is of order 0.2% for measurements below 35 keV. Above this energy the declining x-ray flux and detector efficiencies leads to higher uncertainty levels. Symbols as for Fig. 3.

addition to these apertures, thirty attenuating foils were mounted on the perimeter of the daisy wheels and these too could be placed in the path of the beam by suitable rotation of the daisy wheel. The foil thicknesses were chosen to span approximately 3 orders of magnitude in x-ray attenuation, $\left[\frac{\mu}{\rho}\right][\rho t]$.

III. DETERMINING THE MASS ATTENUATION COEFFICIENT

A. Intensity measurements

The attenuations of the tin foils were measured and analyzed in a manner similar to that reported in [20]. Accordingly, we report here only the major variations from that work.

Figure 3 shows the attenuations $\left[\frac{\mu}{\rho}\right][\rho t]$ of the tin foils, calculated using Eqs. (2)-(5) of [20]. The attenuation is observed to rise by a factor of 6 at the absorption edge, at about 29.2 keV. Following this edge, there is a steady decrease in the attenuation until a discontinuity is observed at about 40 keV. This discontinuity has resulted from the transmission of the $\frac{3}{4}$ harmonic of the desired beam energy through the second crystal pair, as will be discussed in Sec. V. At energies higher than 42 keV, the smooth decline of the mass attenuation coefficientis reestablished. Measurements recorded with different apertures of various diameters placed between the absorber and the ion chambers cannot be resolved on this figure, indicating the high level of consistency of the data and the low level of scattering.

Figure 4 shows the determined uncertainties of each attenuation measurement due to counting statistics for each sample thickness or aperture setting, and hence the experimental precision at each point. Investigation of the statistical quality of a data set and the optimization of ion chambers has been discussed earlier [30,31]. In the energy range from 29 keV to 35 keV these component consistencies are gener-

ally below 0.2% for measurements recorded using the optimum foil thickness. If each aperture setting is consistent, then the weighted mean will have a correspondingly improved precision. The uncertainties in the measured attenuations increase rapidly for measurements above about 42 keV, due to the rapid decrease in the source intensity combined with the declining detector efficiencies and beam flux, as discussed in the text. This decline in precision was of course anticipated; a key question was where the statistical limit would dominate.

B. A full-foil absolute measurement of the mass attenuation coefficient

We summarize our use of a full-foil x-ray mapping technique to determine the mass attenuation coefficient of a reference foil to high accuracy. This technique has been used in [20] for molybdenum and is discussed in detail in [32].

In the full-foil mapping technique an *attenuation profile* of the sample plus holder $\left(\left[\frac{\mu}{\rho}\right][\rho t]_{xy}\right)_{S+H}$ is determined by performing a raster measurement of the attenuation at (x, y) locations across the entire sample mounted in a holder. The holder contribution to the attenuation profile is determined by use of a fitting routine. The holder contribution was always less than 20% of the sample attenuation. Subtraction of the fitted holder profile from the total measured profile then produces an attenuation profile of the sample, $\left(\left[\frac{\mu}{\rho}\right][\rho t]_{xy}\right)_S$. The current work differs significantly from earlier work [20,32] due to the use of a 4-mm wide x-ray beam in this experiment in order to optimize statistics.

The 50-μm absorber was mapped with the x-ray beam according to the full-foil mapping procedure at a nominal energy of 29.71 keV (the calibrated energy, discussed below, is 29.693 keV). Measurements were made at about $28 \times 13 = 364$ locations across the surface of the foil, taking 2–3 hours to accomplish. Measurements were made at 2 mm intervals in the horizontal x direction in order to oversample the attenuation profile. Figure 5 shows the measured attenuation profile of the sample plus holder. The measurements are smoothly continuous across the surface of the sample plus holder.

The 29.71 keV attenuation profile has been fitted with a function which models the attenuation profile of the foil plus holder at every measured location to enable subtraction of the holder component. The function (described in [32]) predicts the attenuation profile for a foil plus holder measured using a 1 mm $\times$ 1 mm beam. That function was modified to predict the attenuation profile measured using a N mm $\times$ 1 mm beam ($N \in \{\mathbb{I}\}, N \geq 1$) by evaluating the logarithmic average of N neighboring values of the predicted 1 mm $\times$ 1 mm attenuation according to

$$\left\{\left[\frac{\mu}{\rho}\right][\rho t]\right\}_{N \times 1, x, y} = -\ln\left(\frac{1}{N}\sum_{n=1}^{N} \exp\left\{-\left[\frac{\mu}{\rho}\right]\right.\right.$$
$$\left.\left.\times[\rho t]\right\}_{1 \times 1, x+n-\frac{N+1}{2}, y}\right), \quad (1)$$

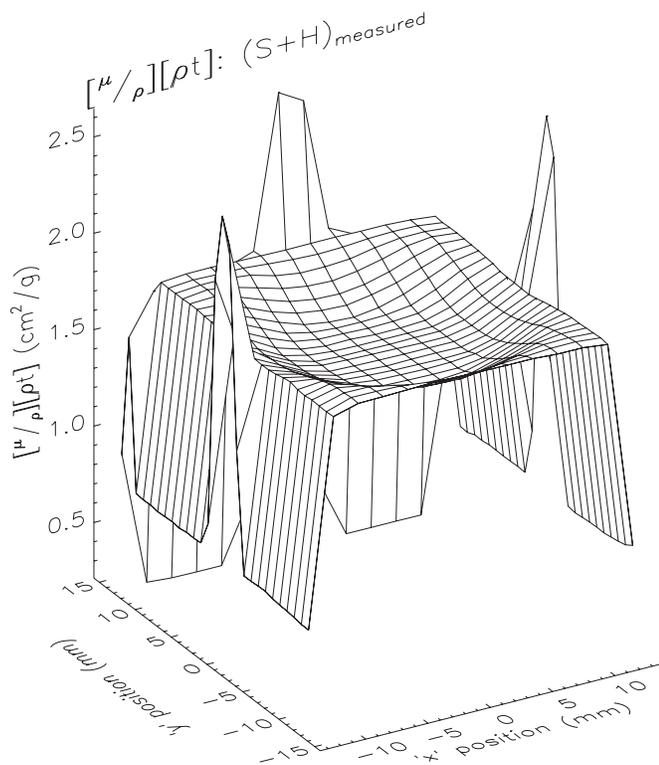where the subscripts refer to the dimensions of the beam and

FIG. 5. The attenuation profile measured using x rays of energy 29.71 keV. The smoothness of the attenuation profile indicates the good statistical level associated with these measurements. The spikes outside the sample edges indicate the locations of metal mounting screws.
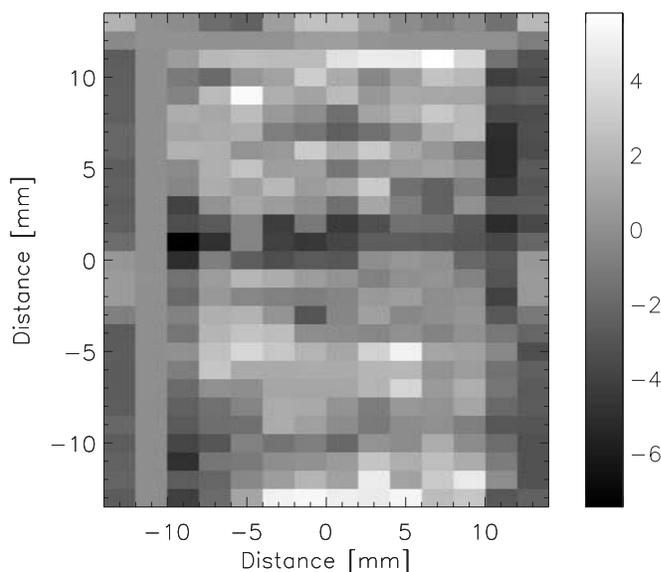

FIG. 6. The residuals of the fit of the 4-mm-wide x-ray beam to the attenuation profile measured at 29.71 keV. Measurements were made every 2 mm in the horizontal and every 1 mm in the vertical. The absence of any structure following the shape of the holder indicates that the holder attenuation profile has been correctly modeled. The regions of middle grey on the left- and right-hand sides and in the top two rows are the points at the foil edge which have been excluded from the fit. The horizontal structure in the residuals implies real structure in the attenuation profile.

the x and y ordinates of the prediction, respectively. The logarithmic averaging in Eq. (1) describes the real averaging of the attenuation over the measured area that occurs when the beam is of uniform intensity. When the beam intensity is nonuniform, Eq. (1) should be weighted by the beam intensity at each point.

The effect of slight beam intensity nonuniformities over a small (1 mm^2) beam is discussed in [20]: however, the degree of the intensity nonuniformity might be more significant here and is discussed in [33]. We have used a four-reflection monochromation system with a 4-mm-wide aperture to define the beam footprint, so the highly directional nature of the x-ray beam might yield a significant decrease of the beam intensity at locations away from the optic axis. However, we find that the observed data is completely consistent with a uniform 4 mm $\times$ 1 mm footprint corresponding to the aperture and for example completely inconsistent with a 2 mm $\times$ 1 mm or a 5 mm $\times$ 1 mm footprint.

The distribution of the residuals—the difference between the fitted and measured attenuation profiles, scaled by the measurement uncertainty (see Eq. (9), Ref [32])—provides sensitive indication of the quality of the fitting model. A systematic distribution of the residuals could indicate a serious model failure [32]. Figure 6 shows the distribution of the residuals for the fit using the 4 mm beam width. The residuals show no circular pattern, confirming that the location and thickness of the holder have been modeled to within the statistical accuracy of the measurements.

The values of the mass attenuation coefficient determined assuming 4-mm-wide beams are consistent within the fitting and measurement uncertainties. All other aspects of the measurement are well behaved. We therefore obtain $\left[\frac{\mu}{\rho}\right]$ $=(44.057 \pm 0.021)$ cm^2/g for the reference point of the sample within the beam. A small correction to this value will be described in Sec. III D.

C. Scaling other mass attenuation coefficients

Figure 7 presents mass attenuation coefficients determined by dividing the measured attenuations by the average integrated column density of the appropriate foil. These results show good consistency and statistical quality. However, the average thickness does not accurately reflect the actual thickness of the foil in the x-ray beam. It is therefore necessary to determine the integrated column density or effective thickness of a particular sample in the beam from the absolute value determined by the full-foil mapping.

Figure 8 presents the percentage deviation of the mass attenuation coefficients from their weighted mean at each energy, after determining the local foil integrated column densities. This is the uncertainty estimate for the particular measurement. The uncertainty in the weighted mean varies from 0.04–0.2 % at energies below 40 keV and generally below about 1% for the measurements made at higher energies. The nominal Goodfellows estimates of average foil thickness have been corrected by 0.6%, 0.37%, 0.28%, 0.16%, 0.04%, −0.4%, and −1.25%, respectively, to obtain the actual effective thicknesses at the points measured in the
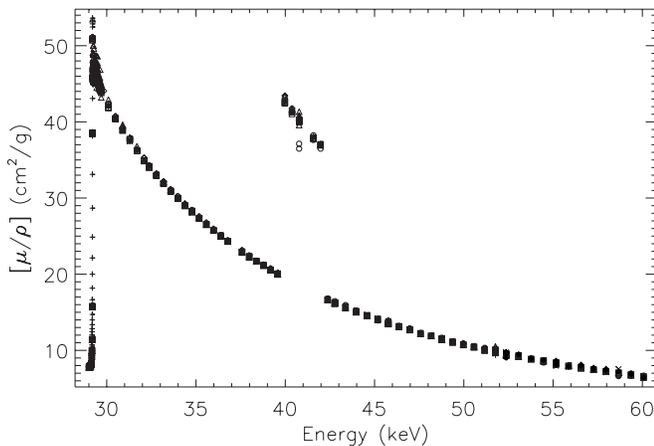
FIG. 7. The mass attenuation coefficients determined by use of the average integrated column density. Symbols as for Fig. 3. The energy axis is given by the nominal setting, as yet uncorrected. Overall consistency on this scale is excellent.

beam. These corrections are in good agreement with observed variation of thickness across the foils.

D. Dark current and the treatment of detector noise

Figure 8 shows systematic variation between measurements using samples of very different thickness, which thus can assess the effect of a variety of "thickness effects" on the measurement. The absence of systematic deviations ($s.d.$) in Fig. 8 indicates that systematic effects are only minor.

However, there is one key systematic signature in the variation between results obtained using different sample thicknesses. This is due to an error of the dark current esti-
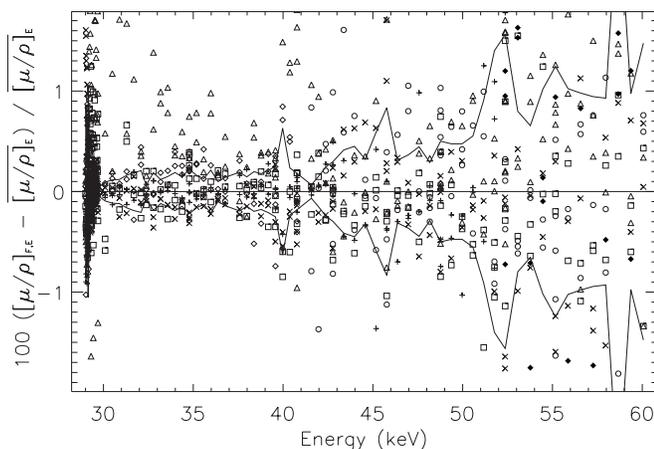

FIG. 8. Percentage deviation of the mass attenuation coefficients from their weighted mean at each energy, after determining the local integrated column densities. There is a complex of deviations around the absorption edge at about 29.2 keV, as discussed in the text. The gradual increase of the deviations as the photon energy increases above about 40 keV is consistent with the lower precision of these measurements. The line indicates the $1\text{-}\sigma_{s.e.}$ variation of the weighted mean, and hence a measurement precision of about 0.04–0.2 % below 40 keV, rising to about 1% at higher energies. Symbols as for Fig. 3.
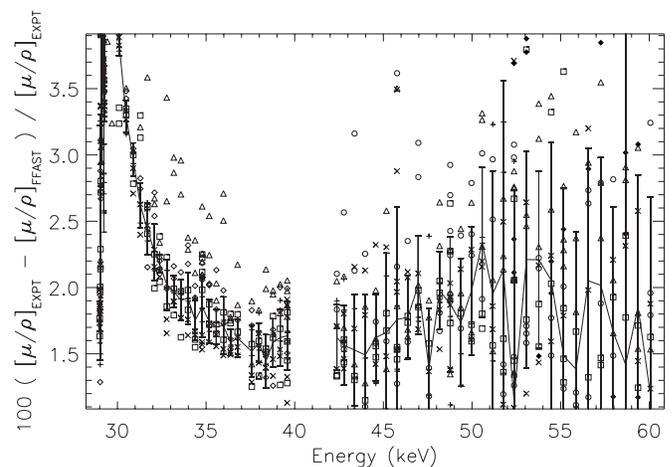

FIG. 9. Percentage difference between the measured mass attenuation coefficients and the FFAST tabulation. By comparing the measured values with a smooth and near-lying result we are able to examine closely the trend of the measured values. This plot demonstrates that away from the edge the trend of the measured values is continuous and smooth to within the estimated uncertainties. Symbols as for Fig. 3.

mates, or in other words a small variation of the actual electronic noise with time. We have fitted for the effect of this dark current variation in the downstream ion chamber, using Eq. (A4) of Ref. [20]. The typical fitted dark current noise level was around 1770 counts/s, compared with a typical directly (but infrequently) measured dark current level of 1700 counts/s±100 counts/s, which is within one standard error ($s.e.$) uncertainty of the dark current in this ion chamber. Although the weighted mean of the corrected values does not change by more than the uncertainty of the measurements, the χ_r^2 reduces from 1.15 to 1.09 after this systematic is corrected for, and the systematic pattern from thin to thick foils is eliminated, indicating that the correction is real. The correction is near the level of the measurement uncertainty, and reaches $1\sigma_{s.e.}$ for the full-foil mapping value at 29.71 keV.

We have included half of the correction to the dark current level in quadrature in the uncertainty estimates. This additional uncertainty component expresses the limiting uncertainty of the measurement without assuming a particular cause, but in fact only becomes barely significant at 29.71 keV.

The total $\sigma_{s.d.}$ uncertainty of each result is then typically below 0.07%. At a number of energies between 25 keV and 30 keV the uncertainty associated with the measurement rises due to instabilities in the apparatus and adjustments of the settings made during the course of the experiment, but these are characterized at every point. The variations in result occurring near the absorption edge remain, possibly due to energy instability or drift, and this has naturally resulted in a slight increase in the $\sigma_{s.d.}$ uncertainty in that region.

In order to examine closely the smoothness of the measurements, we calculate the percentage difference between the measured values and a near lying and smooth function. In Fig. 9 we have used for this purpose the interpolated results of the FFAST calculation. The measured values fall on a con-

tinuous and smooth curve to within the determined uncertainty. The correspondence between the measurement variation and the uncertainties confirms the procedure used to estimate the uncertainties.

E. Other possible signatures and their treatment

We expect that x-ray harmonic energy components will have negligible effect on the measured values due to the method of monochromation employed in this investigation, the intrinsic bending-magnet spectrum, and the harmonic rejection resulting from the ion-chamber efficiencies. This expectation is confirmed by the absence in Fig. 8 of the corresponding systematic signatures at lower energies or for different foil thicknesses.

The shiny appearance of the tin foils indicated that they were significantly smoother than their molybdenum counterparts [20]. This was confirmed by measuring the tin absorbers at several locations across their surface using an atomic force microscope. Any effects of roughness were less than those for molybdenum, for which roughness effects were not detectable [20]. The experimental geometry for the measurement was similar to that in earlier work [1,2,34]. The approach developed in [35] confirms that the effect of fluorescence and other secondary radiation is not significant due to the high degree of beam collimation.

X-ray bandwidth can have an appreciable effect on the measured values in regions of high attenuation gradient (i.e., on the absorption edge and in the XAFS region). Measurements with samples of various thicknesses were made at energy intervals down to 8 eV. Due to the gradient-correlated nature of the bandwidth effect, these few edge measurements provide a weak constraint upon the bandwidth and we observe no effect on the measured mass attenuation coefficients. We have a very highly monochromated beam, even by third-generation synchrotron standards. Two double-reflection monochromators in a $(+--+)$ arrangement (dispersive geometry—see Fig. 2) results in a beam of very narrow bandwidth [36,37]. Hence we expect the negligible effect of the bandwidth as is observed.

IV. DETERMINATION OF X-RAY PHOTON ENERGIES

To determine accurate x-ray energies we have measured the angles of a series of $\{h,h,h\}$ reflections from a germanium single crystal (see Fig. 2) using the same routines and intensity optimization procedures as for earlier measurements with molybdenum. Similar issues with detector saturation and analyzer crystal defects are observed [20]. Accordingly, similar analysis is used to determine the photon energies for this experiment and we present the results here. The logic was detailed in [20].

Figure 10 presents the determined photon energies. The error bars indicate x-ray energies determined from the locations of the leading edge and the center of mass of the measured reflections. The solid line on this plot indicates the result of fitting a modified Bragg function [see [20], Eq. (11)] to the directly determined energies. The χ_r^2 of the fit is about 3.1 and the estimated energy uncertainty is of the order of
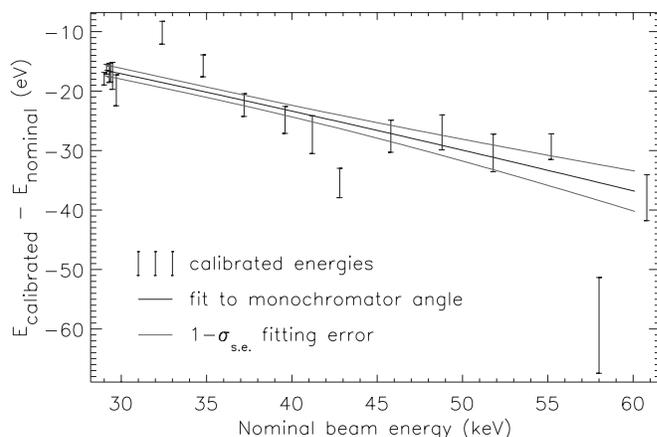

FIG. 10. Determination of the photon energies. The error bar markers shown here indicate the result of direct energy determination by measuring Bragg angles of a number of reflections from a (1,1,1)-oriented germanium crystal. The dark line describes the result of fitting a Bragg function to the monochromator angle and the directly determined energies. The light gray lines surrounding this line indicate the 1-$\sigma_{s.e.}$ uncertainty of the calibrated energy, determined using the covariant error matrix multiplied by $\sqrt{\chi_r^2}$.

1–4 eV. This photon energy accuracy does not limit the mass attenuation results except in regions of high mass attenuation coefficient gradient immediately at the absorption edge.

V. RESULTS FROM THE $\frac{3}{4}$ ENERGY DATA

The discontinuity in the mass attenuation coefficients observed between 40 keV and 42 keV is due to the spurious reflection of $\frac{3}{4}$ energy x rays from planes within the downstream $\{3,3,3\}$ monochromator.

The x-ray energy was selected by tuning the upstream crystal so that the x-rays reflected from the $\{4,4,4\}$ planes of silicon were of the desired energy. When this is done, x rays of all allowed harmonic energies are also transmitted into the beam. Unwanted harmonic energies are then removed by reflecting this partially monochromated beam from the $\{3,3,3\}$ planes of a second downstream silicon crystal. The downstream channel-cut monochromator crystal was tuned to optimize the reflected x-ray intensity by scanning it through a small range of angles about the Bragg angle corresponding to the $\{3,3,3\}$ planes. The peak intensity was identified from the scan, and the crystal was then set at the angle corresponding to the peak intensity.

Figure 11 presents the tuning curves recorded between 39.2 keV and 42.8 keV. The ordinate presents the recorded count rate, with all plots sharing the same scale. The abscissa is the angular location of the downstream monochromator. All tuning curves show a peak in the intensity occurring at the center of the range of the scan. This centered peak is due to the reflection of x rays of the desired beam energy, free of harmonics: its reproducible presence in the center of the scan range proves the alignment and tracking accuracy of the goniometer and the accurate prediction of its location by Bragg's law.
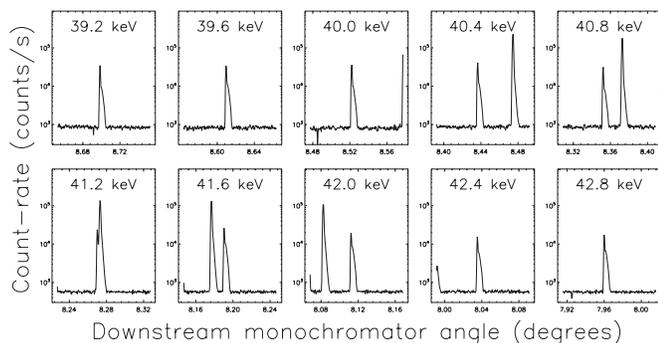
FIG. 11. Tuning curves for the downstream crystal over the energy range from 39.2–42.8 keV. The abscissa is common, showing the intensity (on a logarithmic scale) recorded using an ion chamber located downstream from the second monochromator. The ordinate shows the angular location of the downstream monochromator. The stability of the intensity peak located in the center of the scanned region is due to our scanning over a constant but narrow range about the predicted Bragg angle; the tuning process was designed to optimize this central peak. The second peak is discussed in the text.

The tuning curve taken at 40.0 keV shows a spurious peak entering the high-angle (right-hand) side of the plot. Although the spurious peak is not fully within the scan range, its intensity is greater than that of the central peak and thus unfortunately our automated tuning algorithm interpreted this spurious peak to be the desired reflection, and its intensity was optimized for the attenuation measurement. In subsequent tuning curves the spurious peak moves rapidly across the scan region relative to the position of the central peak. At 42.4 keV, the intensity of the spurious peak decreases below that of the central peak, and the central peak is again correctly optimized. The optimization of the spurious reflection coincides exactly with the discontinuities in the measured attenuations as is evident in Fig. 3.

The values of the mass attenuation coefficients determined at energies between 40.0 keV and 42.0 keV are similar to those measured at energies between 30.0 keV and 31.5 keV, confirming that the energy of the x rays comprising the spurious reflection is $\frac{3}{4}$ of the desired beam energy. Such an occurrence is not unlikely, requiring only an accidental reflection of the $\frac{3}{4}$ energy x rays by a set of planes within the channel-cut $\{3,3,3\}$ monochromator.

We therefore multiply the defined energy calibration for these few points by $\frac{3}{4}$ to give the photon energy for the affected measurements. This assumes that differential shifts from the energy dependence of diffraction—such as refractive index and depth penetration corrections—are not significant over these energies (typically this contributes a shift at the 20–50 part per 10^6 level or approximately $0.4 - 1$ eV shift in defined energy, consistent with the energy uncertainty).

Figure 12 compares the determined values of the mass attenuation coefficient for the incorporated and regular measurements. Values are indicated by their uncertainties in $\left[\frac{\mu}{\rho}\right]$. The large diamond marker indicates the value directly determined using the full-foil mapping procedure. The incorporated measurements are indicated by arrows whose labels give their uncorrected nominal energies. These measure-
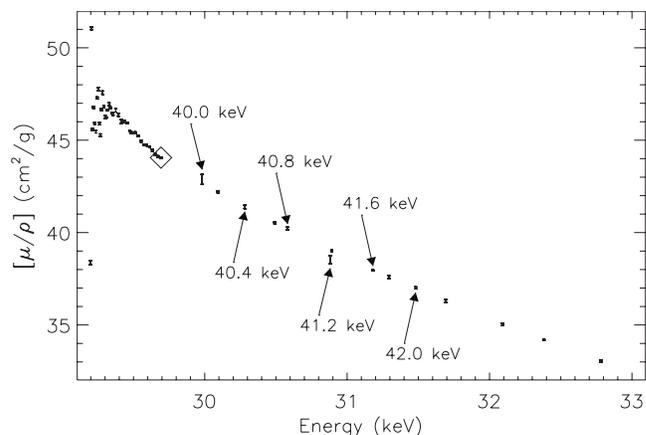

FIG. 12. Incorporation of the $\frac{3}{4}$ energy measurements and comparison to other results in the same energy region. The incorporated values agree with the regular measurements to within their 0.1–0.5 % uncertainties, verifying that this beam is exactly $\frac{3}{4}$ of the energy implied by the position. The measurement made at nominal energy 41.2 keV is inconsistent with the trend of the other values due to the significant fraction of the 41.2 keV photons in the beam (cf. Fig. 11). This single datum has therefore been excluded from the data set.

ments are entirely consistent with the trend of the regular measurements, except for the value at the nominal energy of 41.2 keV. The beam used for 41.2 keV is composed of a mixture of third-and fourth-order photons, and we therefore exclude this point from the data set.

All incorporated measurements of Fig. 12 are consistent with the trend of the regular measurements to within their uncertainties of between 0.07% and 0.6%. The level of agreement shown here confirms the $\frac{3}{4}$ energy hypothesis and provides a dramatic demonstration of the reproducibility of our measurements within their uncertainties.

VI. TABULATION OF THE RESULTS

Table I presents the values of the mass attenuation coefficients between 29 keV and 60 keV.

The calibrated photon energy (in keV) is followed by the uncertainty in the last significant figures presented in parentheses. The mass attenuation coefficient $\left[\frac{\mu}{\rho}\right]$ (in cm²/g) is similarly given with its uncertainty. In the third column we present the percentage uncertainty in the mass attenuation coefficient. The values in the second and third columns are determined from the weighted mean of the measurements made with a variety of apertures and foil thicknesses. The weighted mean typically involved about 10 individual measurements, and hence if each had similar statistical quality and consistency, the precision of the pooled result could be reduced by just over a factor of 3. At a number of energies in the XAFS region only one measurement is used for efficiency, and these naturally have larger uncertainties. The uncertainty in the mass attenuation coefficient was generally evaluated from $\sigma_{s.d.}$ defined in Eqs. (A2) and (A3) of [20]. A detail of the mass attenuation coefficients measured in the region of the absorption edge is plotted as a function of energy in Fig. 13.

TABLE I. Mass attenuation coefficients $\left[\frac{\mu}{\rho}\right]$ and the imaginary component of the atomic form factor f_2 as a function of x-ray energy, with one standard error uncertainties in the least significant digits indicated in parentheses. We present also the percentage uncertainty in the mass attenuation coefficients, $\sigma\left[\frac{\mu}{\rho}\right]/\left[\frac{\mu}{\rho}\right]$. Uncertainty in f_2 includes the measurement uncertainty and the difference between major tabulations of the total Rayleigh plus Compton scattering cross sections. Values of f_2 in the energy range of 29.1 keV–30 keV are affected by solid-state effects.

Energy (keV)	$\left[\frac{\mu}{\rho}\right]$ (cm²/g)	$\sigma\left[\frac{\mu}{\rho}\right]/\left[\frac{\mu}{\rho}\right]$	f_2 (e/atom)
29.00351(92)	7.8285(97)	0.12%	0.5740(23)
29.02351(92)	7.856(68)	0.86%	0.5767(59)
29.04350(92)	7.859(56)	0.71%	0.5774(51)
29.06348(92)	7.877(19)	0.24%	0.5794(27)
29.08347(92)	7.915(59)	0.75%	0.5829(53)
29.10345(92)	8.018(46)	0.57%	0.5918(43)
29.12345(92)	8.167(28)	0.34%	0.6045(31)
29.13344(92)	8.288(22)	0.27%	0.6147(28)
29.14344(92)	8.416(89)	1.1%	0.6254(76)
29.15342(92)	8.627(83)	0.96%	0.6431(72)
29.16341(92)	9.004(78)	0.87%	0.6743(68)
29.16442(92)	9.2723(97)	0.10%	0.6964(23)
29.16542(92)	9.395(76)	0.81%	0.7065(66)
29.16642(92)	9.422(75)	0.80%	0.7088(65)
29.16742(92)	9.526(75)	0.78%	0.7174(65)
29.16841(92)	9.586(74)	0.77%	0.7223(65)
29.16942(92)	9.704(74)	0.76%	0.7321(64)
29.17041(92)	9.758(73)	0.75%	0.7365(64)
29.17142(92)	9.868(73)	0.74%	0.7456(64)
29.17241(92)	9.991(13)	0.13%	0.7558(24)
29.17342(92)	10.109(72)	0.71%	0.7655(63)
29.17541(92)	10.395(71)	0.68%	0.7891(62)
29.17641(92)	10.568(70)	0.66%	0.8034(62)
29.17741(92)	10.776(70)	0.65%	0.8206(61)
29.18041(92)	11.481(14)	0.12%	0.8787(24)
29.18241(92)	12.079(69)	0.57%	0.9280(61)
29.18340(92)	12.476(68)	0.54%	0.9607(60)
29.18441(92)	12.887(68)	0.53%	0.9945(60)
29.18540(92)	13.413(67)	0.50%	1.0379(59)
29.18640(92)	14.041(66)	0.47%	1.0896(59)
29.18741(92)	14.762(67)	0.45%	1.1491(59)
29.18840(92)	15.803(18)	0.12%	1.2349(26)
29.18941(92)	16.711(66)	0.39%	1.3096(58)
29.19040(92)	18.226(65)	0.36%	1.4344(58)
29.19140(92)	20.067(65)	0.32%	1.5861(58)
29.19241(92)	22.202(65)	0.29%	1.7620(58)
29.19340(92)	24.943(65)	0.26%	1.9878(58)
29.19440(92)	28.765(65)	0.23%	2.3026(58)
29.19540(92)	33.208(67)	0.20%	2.6687(59)
29.19640(92)	38.36(11)	0.28%	3.0930(92)

TABLE I. (*Continued.*)

Energy (keV)	$\left[\frac{\mu}{\rho}\right]$ (cm²/g)	$\sigma\left[\frac{\mu}{\rho}\right]/\left[\frac{\mu}{\rho}\right]$	f_2 (e/atom)
29.19740(92)	43.214(70)	0.16%	3.4930(61)
29.19839(92)	47.893(70)	0.15%	3.8785(62)
29.19940(92)	51.164(72)	0.14%	4.1481(63)
29.20040(92)	53.026(80)	0.15%	4.3016(69)
29.20139(92)	53.771(84)	0.16%	4.3632(73)
29.20240(92)	53.433(76)	0.14%	4.3354(66)
29.20340(92)	52.616(76)	0.14%	4.2683(66)
29.20439(92)	51.020(78)	0.15%	4.1369(67)
29.20839(92)	47.343(72)	0.15%	3.8346(63)
29.20939(92)	46.753(73)	0.16%	3.7861(64)
29.21039(92)	46.190(67)	0.15%	3.7398(59)
29.21139(92)	45.895(69)	0.15%	3.7156(61)
29.21239(92)	45.567(43)	0.095%	3.6888(41)
29.21339(92)	45.626(71)	0.16%	3.6937(62)
29.21439(92)	45.678(66)	0.14%	3.6982(58)
29.21539(92)	45.829(67)	0.15%	3.7107(59)
29.21739(92)	46.352(71)	0.15%	3.7541(62)
29.21839(92)	46.528(65)	0.14%	3.7687(58)
29.21939(92)	46.725(68)	0.14%	3.7851(60)
29.22038(92)	46.754(54)	0.12%	3.7876(49)
29.22238(92)	46.994(66)	0.14%	3.8077(58)
29.22338(92)	46.987(66)	0.14%	3.8072(59)
29.22438(92)	46.748(62)	0.13%	3.7876(56)
29.22639(92)	46.641(64)	0.14%	3.7791(57)
29.22738(92)	46.402(66)	0.14%	3.7595(58)
29.22838(92)	45.891(54)	0.12%	3.7175(49)
29.23038(92)	45.443(65)	0.14%	3.6808(58)
29.23138(92)	45.199(64)	0.14%	3.6609(57)
29.23238(92)	45.095(64)	0.14%	3.6524(57)
29.23338(92)	45.026(63)	0.14%	3.6469(56)
29.23438(92)	45.092(63)	0.14%	3.6524(56)
29.23538(92)	45.311(65)	0.14%	3.6706(58)
29.23638(92)	45.439(42)	0.092%	3.6813(41)
29.23738(92)	45.708(64)	0.14%	3.7036(57)
29.23837(92)	45.938(63)	0.14%	3.7227(56)
29.23938(92)	46.161(63)	0.14%	3.7412(56)
29.24037(92)	46.349(63)	0.14%	3.7569(56)
29.24137(92)	46.617(64)	0.14%	3.7791(57)
29.24237(92)	46.839(64)	0.14%	3.7976(57)
29.24337(92)	47.037(63)	0.13%	3.8140(56)
29.24437(92)	47.267(32)	0.067%	3.8331(34)
29.24537(92)	47.532(64)	0.13%	3.8551(57)
29.24636(92)	47.741(64)	0.13%	3.8725(57)
29.24736(92)	47.879(63)	0.13%	3.8840(56)
29.24837(92)	48.022(64)	0.13%	3.8959(57)
29.24936(92)	48.097(65)	0.13%	3.9022(58)
29.25037(92)	48.133(65)	0.13%	3.9053(57)

TABLE I. (*Continued.*)

Energy (keV)	$\left[\frac{\mu}{\rho}\right]$ (cm²/g)	$\sigma\left[\frac{\mu}{\rho}\right]/\left[\frac{\mu}{\rho}\right]$ (e/atom)	f_2
29.25137(92)	47.982(64)	0.13%	3.8930(57)
29.25237(92)	47.749(88)	0.18%	3.8739(76)
29.25337(92)	47.721(64)	0.13%	3.8718(57)
29.25436(92)	47.512(65)	0.14%	3.8547(58)
29.25536(92)	47.169(65)	0.14%	3.8265(58)
29.25636(92)	46.988(65)	0.14%	3.8117(58)
29.25736(92)	46.739(66)	0.14%	3.7912(58)
29.25836(92)	46.464(66)	0.14%	3.7687(59)
29.25936(92)	46.223(65)	0.14%	3.7489(58)
29.26035(92)	45.859(61)	0.13%	3.7190(55)
29.26136(92)	45.773(66)	0.14%	3.7121(58)
29.26236(92)	45.616(67)	0.15%	3.6992(60)
29.26336(92)	45.399(66)	0.15%	3.6815(58)
29.26436(92)	45.365(67)	0.15%	3.6788(59)
29.26535(92)	45.262(68)	0.15%	3.6704(60)
29.26636(92)	45.262(68)	0.15%	3.6705(60)
29.26736(92)	45.303(70)	0.15%	3.6740(61)
29.26836(92)	45.254(44)	0.098%	3.6701(42)
29.26935(92)	45.364(69)	0.15%	3.6793(61)
29.27035(92)	45.516(70)	0.15%	3.6920(61)
29.27135(92)	45.646(73)	0.16%	3.7029(64)
29.27236(92)	45.790(70)	0.15%	3.7149(62)
29.27335(92)	45.994(71)	0.15%	3.7318(62)
29.27435(92)	46.218(74)	0.16%	3.7505(65)
29.27535(92)	46.485(76)	0.16%	3.7727(66)
29.27635(92)	46.643(20)	0.043%	3.7859(27)
29.27735(92)	46.874(77)	0.16%	3.8050(67)
29.27934(92)	47.113(73)	0.15%	3.8251(64)
29.28335(92)	47.631(75)	0.16%	3.8684(66)
29.28435(92)	47.53(10)	0.21%	3.8599(85)
29.28534(92)	47.498(76)	0.16%	3.8577(67)
29.28734(92)	47.425(78)	0.16%	3.8519(68)
29.29134(92)	47.012(80)	0.17%	3.8184(70)
29.29234(92)	46.776(54)	0.11%	3.7989(49)
29.29334(92)	46.715(81)	0.17%	3.7941(70)
29.29434(92)	46.681(82)	0.18%	3.7914(71)
29.29534(92)	46.595(82)	0.18%	3.7844(71)
29.29634(92)	46.604(85)	0.18%	3.7852(74)
29.29734(92)	46.434(84)	0.18%	3.7713(73)
29.29833(92)	46.417(83)	0.18%	3.7701(72)
29.29934(92)	46.379(84)	0.18%	3.7671(73)
29.30033(92)	46.236(39)	0.085%	3.7553(39)
29.30134(92)	46.257(86)	0.19%	3.7572(74)
29.30233(92)	46.240(87)	0.19%	3.7559(75)
29.30333(92)	46.231(87)	0.19%	3.7554(75)
29.30433(92)	46.258(89)	0.19%	3.7577(76)
29.30533(92)	46.231(88)	0.19%	3.7556(76)
29.30633(92)	46.226(89)	0.19%	3.7553(76)
29.30733(92)	46.260(92)	0.20%	3.7583(79)
29.30833(92)	46.197(42)	0.091%	3.7532(41)
29.30933(92)	46.321(96)	0.21%	3.7636(82)
29.31033(92)	46.333(93)	0.20%	3.7647(80)
29.31133(92)	46.366(94)	0.20%	3.7675(80)
29.31233(92)	46.438(98)	0.21%	3.7736(84)
29.31433(92)	46.519(95)	0.20%	3.7806(81)
29.31533(92)	46.582(98)	0.21%	3.7860(83)
29.31632(92)	46.658(97)	0.21%	3.7924(83)
29.31832(92)	46.608(36)	0.077%	3.7885(37)
29.31932(92)	46.79(10)	0.21%	3.8038(85)
29.32033(92)	46.89(10)	0.22%	3.8123(89)
29.32132(92)	46.93(10)	0.22%	3.8155(89)
29.32232(92)	46.96(11)	0.23%	3.8179(94)
29.32332(92)	46.89(11)	0.23%	3.8126(90)
29.32432(92)	46.97(10)	0.22%	3.8195(89)
29.32732(92)	46.95(11)	0.23%	3.8179(91)
29.32832(92)	46.863(41)	0.088%	3.8109(41)
29.32932(92)	46.949(98)	0.21%	3.8182(84)
29.33032(92)	47.00(10)	0.21%	3.8223(86)
29.33132(92)	46.97(10)	0.21%	3.8199(85)
29.33231(92)	46.93(10)	0.21%	3.8171(85)
29.33332(92)	46.96(10)	0.22%	3.8192(87)
29.33432(92)	46.94(10)	0.22%	3.8179(88)
29.33531(92)	46.91(10)	0.22%	3.8161(89)
29.33631(92)	46.89(13)	0.27%	3.814(11)
29.33731(92)	46.85(10)	0.22%	3.8107(88)
29.33832(92)	46.733(44)	0.095%	3.8015(43)
29.33931(92)	46.81(10)	0.22%	3.8079(89)
29.34031(92)	46.77(11)	0.23%	3.8050(91)
29.34131(92)	46.72(11)	0.23%	3.8006(90)
29.34230(92)	46.72(11)	0.23%	3.8008(91)
29.34331(92)	46.68(11)	0.24%	3.7976(94)
29.34431(92)	46.62(11)	0.24%	3.7931(93)
29.34531(92)	46.61(11)	0.23%	3.7923(93)
29.34631(92)	46.57(11)	0.23%	3.7893(93)
29.34731(92)	46.55(11)	0.24%	3.7878(93)
29.34830(92)	46.437(38)	0.082%	3.7783(38)
29.34930(92)	46.49(11)	0.24%	3.7829(97)
29.35031(92)	46.49(11)	0.24%	3.7827(96)
29.35131(92)	46.44(12)	0.26%	3.779(10)
29.35330(92)	46.45(12)	0.25%	3.7803(99)
29.35580(92)	46.341(41)	0.089%	3.7714(40)
29.35830(92)	46.40(14)	0.31%	3.777(12)
29.36080(92)	46.20(13)	0.27%	3.760(11)
29.36829(92)	46.34(11)	0.25%	3.7732(97)

TABLE I. (*Continued.*)

Energy (keV)	$\left[\frac{\mu}{\rho}\right]$ (cm^2/g)	$\sigma\left[\frac{\mu}{\rho}\right]/\left[\frac{\mu}{\rho}\right]$ (e/atom)	f_2
29.37080(92)	46.57(12)	0.25%	3.7925(99)
29.37579(92)	46.563(19)	0.040%	3.7924(27)
29.37829(92)	46.568(98)	0.21%	3.7931(84)
29.38079(92)	46.593(95)	0.20%	3.7955(81)
29.38578(92)	46.595(89)	0.19%	3.7963(77)
29.38828(92)	46.565(86)	0.19%	3.7942(75)
29.39078(92)	46.534(84)	0.18%	3.7919(73)
29.39328(92)	46.455(82)	0.18%	3.7857(71)
29.39578(92)	46.313(28)	0.060%	3.7743(32)
29.39828(92)	46.279(76)	0.16%	3.7717(67)
29.40078(92)	46.232(76)	0.17%	3.7682(67)
29.40327(92)	46.168(74)	0.16%	3.7632(65)
29.40577(92)	46.099(74)	0.16%	3.7578(65)
29.40827(92)	46.029(75)	0.16%	3.7523(66)
29.41076(92)	46.015(74)	0.16%	3.7515(65)
29.41327(92)	45.992(76)	0.17%	3.7499(67)
29.41577(92)	45.960(47)	0.10%	3.7476(44)
29.41826(92)	45.949(77)	0.17%	3.7470(68)
29.42076(92)	45.955(79)	0.17%	3.7478(69)
29.42326(92)	45.938(82)	0.18%	3.7467(71)
29.42576(92)	45.957(84)	0.18%	3.7487(73)
29.42825(92)	45.961(87)	0.19%	3.7493(75)
29.43325(92)	46.032(93)	0.20%	3.7558(80)
29.43575(92)	46.001(56)	0.12%	3.7536(51)
29.43825(92)	46.06(10)	0.22%	3.7592(89)
29.44075(92)	46.11(11)	0.24%	3.7632(93)
29.44324(92)	46.07(11)	0.24%	3.7599(95)
29.44575(92)	46.02(12)	0.25%	3.7566(99)
29.44824(92)	46.01(12)	0.26%	3.756(10)
29.45074(92)	46.02(13)	0.27%	3.757(11)
29.45574(92)	45.919(38)	0.083%	3.7494(38)
29.45824(92)	45.89(14)	0.31%	3.747(12)
29.46074(92)	45.67(14)	0.31%	3.729(12)
29.46573(92)	45.58(15)	0.33%	3.722(13)
29.46824(92)	45.49(15)	0.34%	3.715(13)
29.47073(92)	45.45(16)	0.35%	3.713(13)
29.47323(92)	45.522(34)	0.076%	3.7187(36)
29.48322(92)	45.416(31)	0.069%	3.7111(34)
29.49321(92)	45.394(32)	0.072%	3.7106(35)
29.51320(92)	45.408(46)	0.10%	3.7143(44)
29.52320(92)	45.356(55)	0.12%	3.7113(51)
29.53320(92)	45.245(30)	0.066%	3.7033(33)
29.54318(92)	45.043(54)	0.12%	3.6877(50)
29.55318(92)	44.959(50)	0.11%	3.6820(47)
29.56318(92)	44.783(52)	0.12%	3.6687(49)
29.57317(92)	44.757(30)	0.068%	3.6678(33)
29.59316(92)	44.730(34)	0.075%	3.6680(36)

TABLE I. (*Continued.*)

Energy (keV)	$\left[\frac{\mu}{\rho}\right]$ (cm^2/g)	$\sigma\left[\frac{\mu}{\rho}\right]/\left[\frac{\mu}{\rho}\right]$ (e/atom)	f_2
29.61314(92)	44.670(32)	0.072%	3.6655(35)
29.62314(92)	44.499(48)	0.11%	3.6525(46)
29.63313(92)	44.445(49)	0.11%	3.6493(46)
29.64312(92)	44.381(49)	0.11%	3.6451(46)
29.65311(92)	44.234(39)	0.089%	3.6341(39)
29.66311(92)	44.141(47)	0.11%	3.6276(45)
29.67311(92)	44.120(39)	0.088%	3.6271(39)
29.69310(92)	44.038(32)	0.072%	3.6228(34)
29.98248(98)	42.90(27)	0.63%	3.563(23)
30.09285(91)	42.178(41)	0.098%	3.5148(41)
30.28229(99)	41.381(97)	0.24%	3.4693(86)
30.49260(90)	40.509(45)	0.11%	3.4190(45)
30.5821(10)	40.201(69)	0.17%	3.4026(64)
30.89236(90)	39.010(39)	0.10%	3.3342(41)
31.1817(11)	37.934(30)	0.078%	3.2715(34)
31.29211(90)	37.574(54)	0.14%	3.2516(53)
31.4815(11)	36.994(52)	0.14%	3.2203(52)
31.69187(89)	36.265(66)	0.18%	3.1772(63)
32.09161(89)	35.019(71)	0.20%	3.1055(68)
32.38144(88)	34.174(21)	0.061%	3.0571(30)
32.78119(88)	33.041(56)	0.17%	2.9910(57)
33.18093(88)	31.992(31)	0.095%	2.9303(37)
33.58069(88)	30.983(39)	0.13%	2.8710(44)
33.98045(87)	30.040(51)	0.17%	2.8157(55)
34.38019(87)	29.087(37)	0.13%	2.7573(44)
34.77994(87)	28.250(58)	0.20%	2.7082(62)
35.17969(87)	27.392(40)	0.15%	2.6550(47)
35.57944(88)	26.585(30)	0.11%	2.6051(40)
35.97919(88)	25.823(50)	0.19%	2.5579(57)
36.37893(88)	25.060(26)	0.10%	2.5088(38)
36.77868(89)	24.361(34)	0.14%	2.4647(45)
37.57817(90)	22.995(39)	0.17%	2.3752(50)
37.97792(91)	22.378(31)	0.14%	2.3352(43)
38.37766(92)	21.740(46)	0.21%	2.2915(57)
38.77740(93)	21.183(38)	0.18%	2.2553(50)
39.17714(95)	20.629(40)	0.19%	2.2181(52)
39.57689(96)	20.080(50)	0.25%	2.1802(63)
42.3751(11)	16.732(38)	0.23%	1.9392(55)
42.7748(11)	16.308(47)	0.29%	1.9070(65)
43.3744(12)	15.708(65)	0.41%	1.8613(86)
43.9740(12)	15.136(68)	0.45%	1.8172(91)
44.5736(13)	14.617(49)	0.34%	1.7777(70)
45.1733(13)	14.110(85)	0.60%	1.738(11)
45.7729(14)	13.63(11)	0.82%	1.701(15)
46.3725(14)	13.170(43)	0.33%	1.6630(66)
46.9721(15)	12.755(48)	0.38%	1.6305(72)
47.5717(16)	12.254(54)	0.44%	1.5850(80)

TABLE I.   (*Continued.*)

Energy (keV)	$\left[\frac{\mu}{\rho}\right]$ (cm²/g)	$\sigma\left[\frac{\mu}{\rho}\right]/\left[\frac{\mu}{\rho}\right]$ (e/atom)	f_2
48.1713(16)	11.919(35)	0.30%	1.5603(59)
48.7709(17)	11.520(59)	0.51%	1.5257(89)
49.3705(18)	11.135(54)	0.48%	1.4916(83)
49.9701(18)	10.806(53)	0.49%	1.4643(83)
50.5697(19)	10.505(58)	0.55%	1.4397(90)
51.1693(20)	10.141(92)	0.91%	1.405(14)
51.7689(21)	9.85(14)	1.4%	1.379(21)
52.3685(22)	9.46(15)	1.6%	1.339(22)
53.0680(23)	9.225(74)	0.80%	1.323(12)
53.7675(24)	8.908(59)	0.66%	1.2928(96)
54.4670(25)	8.593(87)	1.0%	1.262(14)
55.1665(26)	8.26(10)	1.2%	1.227(16)
55.8661(27)	7.979(82)	1.0%	1.199(13)
56.5656(28)	7.770(76)	0.98%	1.182(13)
57.2651(29)	7.517(72)	0.95%	1.156(12)
57.9646(30)	7.253(68)	0.94%	1.128(12)
58.6641(31)	7.01(20)	2.9%	1.102(34)
59.3636(33)	6.814(66)	0.97%	1.084(12)
60.0632(34)	6.558(96)	1.5%	1.054(17)

In the fourth column of Table I we present the imaginary component of the atomic form factor f_2, evaluated from

$$f_2 = \frac{EuA\left[\frac{\mu}{\rho}\right]_{p.e.}}{2hcr_e}, \quad (2)$$

where E is the photon energy in eV, u is the atomic mass unit, A the relative atomic mass of tin, h is the Planck constant, c the speed of light, r_e the classical electron radius, and $\left[\frac{\mu}{\rho}\right]_{p.e.}$ is the photoelectric component of the attenuation.
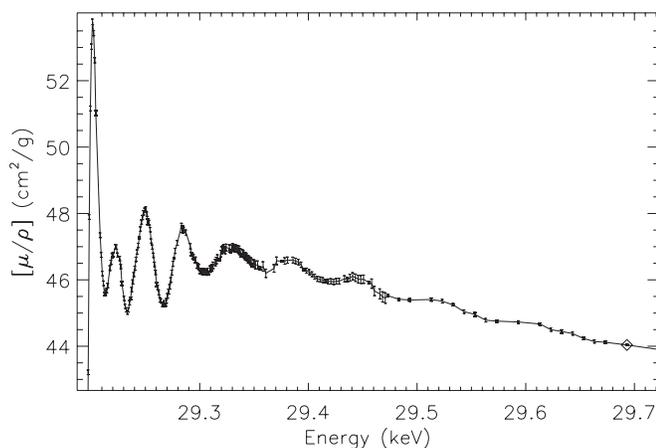

FIG. 13. Detail of the measured mass attenuation coefficients in the region of the XAFS, with error bars giving the absolute accuracy. Usually these standard errors are dominated by the contribution from limitations of precision. Symbols as for Fig. 3.

$\left[\frac{\mu}{\rho}\right]_{p.e.}$ has been evaluated by subtracting the average of the Rayleigh plus Compton contribution as tabulated in XCOM [17,18] and FFAST [14–16]. In parentheses following the reported values is an uncertainty in f_2, evaluated from

$$\sigma_{f_2} = \frac{EuA}{2hcr_e}(\sigma^2_{\left[\frac{\mu}{\rho}\right]} + \Delta^2_{RC})^{1/2}, \quad (3)$$

which includes an uncertainty contribution of half of the difference Δ_{RC} between the two noted tabulated values of the Rayleigh plus Compton contribution.

The use of the photoelectric component of the attenuation determined in this manner is appropriate when Rayleigh and Compton scattering are the only other significant contributions to the total attenuation. This is certainly the case in the energy range covered by this experiment except near the absorption edge and in the region of the XAFS. In these regions the influence of solid-state and bonding effects is naturally substantial.

Estimates of the individual error contributions to the reported values are presented in Table II.

VII. COMPARISON OF THE PHOTOELECTRIC ABSORPTION COEFFICIENT $\left[\frac{\mu}{\rho}\right]_{p.e.}$ WITH TABULATED VALUES

The mass attenuation coefficientcan be written as a sum of photoelectric absorption $\left[\frac{\mu}{\rho}\right]_{p.e.}$, Rayleigh scattering $\left[\frac{\mu}{\rho}\right]_R$, and Compton scattering $\left[\frac{\mu}{\rho}\right]_C$:

$$\left[\frac{\mu}{\rho}\right] \approx \left[\frac{\mu}{\rho}\right]_{p.e.} + \left[\frac{\mu}{\rho}\right] + \left[\frac{\mu}{\rho}\right]_C. \quad (4)$$

We do not discuss other attenuating processes in this summation as they are negligible in the energy region of this experiment.

The results of atomic form-factor calculations can be assessed by comparing the calculated photoelectric absorption coefficients or atomic form factors with our measured values given by the imaginary component of the form factor in the last column of the table. High above the edge these are truly atomic experimental determinations, with often dominant uncertainty arising from the subtraction of the scattering cross sections. This final atomic accuracy, given the assumptions stated, is often 0.1% to 0.2%. Near the edge this result is of course strongly affected by the solid-state interaction, of the order of several percent of more, at least up to an energy of 30–31 keV. This is of course typified by the x-ray absorption fine structure.

In Fig. 14 we present the percentage discrepancy between a variety of commonly used tabulations of $\left[\frac{\mu}{\rho}\right]_{p.e.}$ and our results. Our experimental results form the zero (reference) line, with measurement uncertainties presented as error bars about this zero line. The uncertainty in the subtracted Rayleigh plus Compton cross sections is presented as a shaded region around the zero line. The uncertainty in the subtracted Rayleigh plus Compton cross sections is generally less than our experimental error bars.

At energies above around 45 keV the XCOM and FFAST values are in best agreement, differing by less than 1%. This

TABLE II. Error contributions to the values reported in Table I, with source specified. Further established limits for the systematic uncertainty are quoted here.

Quantity	Estimated magnitude	Contributions and comments
		Away from the absorption edge
$\left[\frac{\mu}{\rho}\right]$	0.04%	accuracy limited by the full-foil mapping technique (section III B)
	$<3\%$	precision, limited by counting statistics
	$<0.03\%$	incorrectly estimated dark current
		Near the absorption edge (29.15 keV–30 keV)
	$<0.01\%$	x-ray bandwidth
E	$0.003-0.007\,\%$	monochromator dispersion function interpolation (section IV)
f_2	$0-0.2-0.4\,\%$	inconsistency of subtracted scattering components (section VI)

difference rises to around 4% at around 35 keV. Our measurements begin to resolve these differences, indicating that the XCOM values exhibit an oscillation in the above-edge region. Such an oscillatory difference of XCOM values from measured values has been observed elsewhere [20] and may be the result of an incompletely converged calculation [14,15]. Such oscillations are often due to inadequate wavefunction representation or a Fourier or other component of the wave-function which has not converged, e.g., in the Hartree iteration. The FFAST tabulation does not show any such
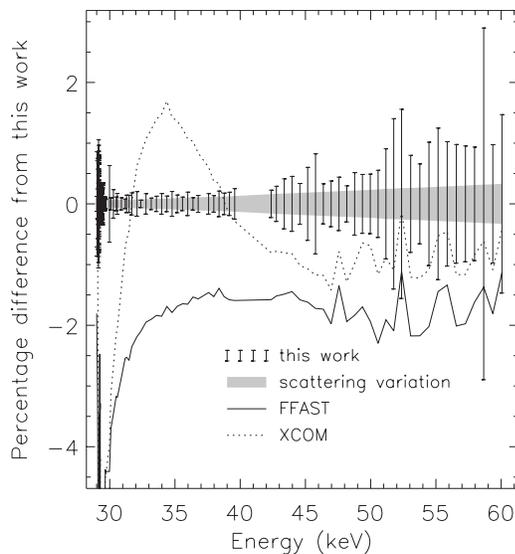

FIG. 14. Percentage discrepancy between various tabulated values of $\left[\frac{\mu}{\rho}\right]_{p.e.}$ and this work. We have determined $\left[\frac{\mu}{\rho}\right]_{p.e.}$ by subtracting the average of the calculated Rayleigh plus Compton scattering cross-sections of FFAST and XCOM from our measured values. The results of this work appear along the zero line, with error bars reflecting experimental uncertainties. The narrow grey region around the zero line represents half of the difference between the Rayleigh plus Compton scattering cross sections Δ_{RC} tabulated in XCOM and FFAST, and reflects the likely error in the absorption coefficient evaluated using these different models. Tabulated values are taken from FFAST [14–16] and XCOM [17,18].

oscillatory behavior, indicating a well-converged calculation.

Both tabulations significantly underestimate $\left[\frac{\mu}{\rho}\right]_{p.e.}$ within around 2 keV of the absorption edge. Previous measurements for copper [1], silver [34], and molybdenum [20] have reported differences between measured values and the FFAST and other tabulations in the region immediately above the absorption edge. Over this region the measured values typically decrease from being 3–5 % higher than the FFAST values to values just above the FFAST values. A similar difference is observed in Fig. 14 for tin.

This systematic difference occurs in the region of the XAFS, which—if resulting from solid-state effects—may indicate that the XAFS is not solely oscillatory, but that it contains an offset term resulting in an enhancement of the attenuation. If this is indeed the case, then it is interesting to ask what factors influence the magnitude of this offset and what additional information can be deduced from accurate measurements of the XAFS offset.

The theoretical accuracy claimed well above the edge is no better than 1%, and near the edge this estimated uncertainty increases. We certainly see that these theoretical estimates are reasonable. The typical discrepancy anticipated by the leading tabulations is clearly confirmed by the experimental data. However, we observe a structural, systematic variation, likely due to a specific cause in the computations. The consistency of this pattern in four elements indicates either a systematic problem with theoretical formalisms or the presence of a previously unrecognized or uncalculated physical contribution to the measured attenuation in this region.

VIII. CONCLUSION

We have determined the mass attenuation coefficients of tin between 29 keV and 60 keV. The measurements are placed on an absolute scale by comparison with the results of a full-foil mapping procedure which has been used to determine the absolute mass attenuation coefficientat a single energy.

Measurements have been made over an extended range of the measurement parameter space. The values obtained from

this extended investigation have been examined for the effect of systematic errors on the measurement. We have corrected a systematic error in the measured values arising from the effect of an incorrectly determined dark current.

The measurements are compared with a variety of predictions of the photoelectric absorption coefficients. These experimental results form a baseline for investigations of tin in this regime. Away from the absorption edge the FFAST tabulation shows a stable 2% difference from our measurements.

Systematic differences between the FFAST calculation and the results of a number of recent experiments are confirmed for tin. The systematic nature of these differences indicates that theoretical approaches need to be refined in certain regions. These discrepancies may indicate new physics, particularly in the above-edge region. Absolute measurements in the near-edge region are of considerable interest in solid-state and bonding studies, and in particular for those wishing to compute, measure or interpret XAFS and x-ray absorption near-edge structure (XANES) on an absolute scale.

[1] C. T. Chantler, C. Q. Tran, Z. Barnea, D. Paterson, D. Cookson, and D. X. Balaic, Phys. Rev. A **64**, 062506 (2001).

[2] C. Q. Tran, C. T. Chantler, Z. Barnea, D. Paterson, and D. J. Cookson, Phys. Rev. A **67**, 042716 (2003); C. Q. Tran, C. T. Chantler, and Z. Barnea, Phys. Rev. Lett. **90**, 257401 (2003); C. T. Chantler and Z. Barnea, J. Phys.: Condens. Matter **11**, 4087 (1999)

[3] M. S. Freedman and F. T. Porter, Phys. Rev. A **6**, 659 (1972).

[4] D. W. Lindle *et al.*, Phys. Rev. A **38**, 2371 (1988).

[5] P. Weightman, E. D. Roberts, and C. E. Johnson, J. Phys. C **8**, 550 (1975).

[6] M. O. Krause and J. H. Oliver, J. Phys. Chem. Ref. Data **8**, 329 (1979).

[7] Y. Joly, D. Cabaret, H. Renevier, and C. R. Natoli, Phys. Rev. Lett. **82**, 2398 (1999).

[8] D. Sayers, E. Stern, and F. Lytle, Phys. Rev. Lett. **27**, 1204 (1971).

[9] Y. Joly, Phys. Rev. B **63**, 125120 (2001).

[10] E. C. Cosgriff, C. T. Chantler, C. Witte, L. Smale, and C. Q. Tran, Phys. Lett. A **343**, 174 (2005).

[11] C. Witte, C. T. Chantler, E. C. Cosgriff, and C. Q. Tran, Radiat. Phys. Chem. **75**, 1582 (2006).

[12] C. T. Chantler, C. Q. Tran, D. Paterson, D. J. Cookson, and Z. Barnea, Phys. Lett. A **286**, 338 (2001).

[13] L. F. Smale, C. T. Chantler, M. D. de Jonge, Z. Barnea, and C. Q. Tran, Radiat. Phys. Chem. **75**, 1559 (2006).

[14] C. T. Chantler, J. Phys. Chem. Ref. Data **29**, 597 (2000).

[15] C. T. Chantler, J. Phys. Chem. Ref. Data **24**, 71 (1995).

[16] C. T. Chantler *et al.*, *X-Ray Form Factor, Attenuation and Scattering Tables (version 2.0)*. (National Institute of Standards and Technology, Gaithersburg, MD, 2003), http://physics.nist.gov/ffast

[17] M. J. Berger, J. H. Hubbell, S. M. Seltzer, J. S. Coursey, and D. S. Zucker, http://physics.nist.gov/xcom

[18] M. J. Berger and J. H. Hubbell, NIST Standard Reference Database 8, **87**, 3597 (2004).

[19] http://physics.nist.gov/PhysRefData/Note/fig1.html

[20] M. D. de Jonge, C. Q. Tran, C. T. Chantler, Z. Barnea, B. B. Dhal, D. J. Cookson, W. K. Lee, and A. Mashayekhi, Phys. Rev. A **71**, 032702 (2005).

[21] J. H. Hubbell, NIST Internal Report5437, 1994 (unpublished).

[22] J. H. Hubbell, J. S. Coursey, J. Hwang, and D. S. Zucker, http://physics.nist.gov/photoncs

[23] D. C. Creagh and J. H. Hubbell, Acta Crystallogr., Sect. A: Found. Crystallogr. **43**, 102 (1987).

[24] D. C. Creagh and J. H. Hubbell, Acta Crystallogr., Sect. A: Found. Crystallogr. **46**, 402 (1990).

[25] C. T. Chantler, Z. Barnea, C. Q. Tran, J. B. Tiller, and D. Paterson, Opt. Quantum Electron. **31**, 495 (1999).

[26] http://www.espimetals.com/

[27] http://www.espimetals.com/metals/molybdenum.pdf

[28] M. A. Beno *et al.*, Nucl. Instrum. Methods Phys. Res. A **467-8**, 699 (2001).

[29] C. Q. Tran *et al.*, X-Ray Spectrom. **32**, 69 (2003).

[30] C. T. Chantler, C. Q. Tran, D. Paterson, Z. Barnea, and D. J. Cookson, X-Ray Spectrom. **29**, 449 (2000).

[31] C. T. Chantler, C. Q. Tran, D. Paterson, D. J. Cookson, and Z. Barnea, X-Ray Spectrom. **29**, 459 (2000).

[32] M. D. de Jonge, Z. Barnea, C. T. Chantler, and C. Q. Tran, Meas. Sci. Technol. **15**, 1811 (2004).

[33] M. D. de Jonge, Ph.D. thesis, University of Melbourne, Australia, 2005.

[34] C. Q. Tran *et al.*, J. Phys. B, **38**, 89 (2005).

[35] C. Q. Tran, M. D. de Jonge, Z. Barnea, and C. T. Chantler, J. Phys. B **37**, 3163 (2004).

[36] J. W. DuMond, Phys. Rev. **52**, 872 (1937).

[37] S. Kraft, J. Stümpel, P. Becker, and U. Kuetgens, Rev. Sci. Instrum. **67**, 681 (1996).